Focus Section: Intraplate Earthquakes

Folding Growth Pattern of the Southern Tian Shan: Insights from the 2024 M_w 7.0 Wushi Earthquake and 2020 M_w 6.0 Jiashi Earthquake, Western China

Zhidan Chen[1], Nan Fang[1], Wenbin Xu[*1], Yuan Yao[2], Peng Zhou[1], Lei Xie[1], and Lei Zhao[1]

Abstract

The 2024 M_w 7.0 Wushi and 2020 M_w 6.0 Jiashi earthquakes, two recent large events in the southern Tian Shan, provide rare opportunities for understanding the seismotectonic deformation patterns in compressional orogenic regimes. Here, we utilize Sentinel-1 satellite radar images and Differential Interferometric Synthetic Aperture Radar techniques to map coseismic deformation fields for the 2024 Wushi and 2020 Jiashi earthquakes, occurring at the front and root of the Kepingtage fold-and-thrust belt, respectively. A modified Bayesian nonlinear method is utilized to simultaneously invert fault geometry parameters and slip distributions. Our findings show that both Wushi and Jiashi earthquakes are predominantly characterized by reverse/thrust motions with minor strike-slip components. The spatial continuity of the interferometric fringes and coseismic deformation fields suggests shallow (< 5 km depth) folding deformation in response to deeper reverse/thrust faulting. Specifically, the Wushi earthquake produced a high-angle fault-propagation fold, with fault-slip penetrating into the crystalline basement, whereas the Jiashi earthquake formed a low-angle detachment fold developed within the cover layer. The M_w 5.7 aftershock following the Wushi mainshock compensated for the shallow coseismic slip deficit and generated positive flowerlike ruptures superimposed on the pre-existing mainshock fold deformation, explaining the observed opposite dip direction of the aftershock rupture compared to the mainshock mechanism. These two fold-type earthquakes demonstrate the dominance of folding deformation in accommodating crustal shortening and orogenic growth in the southern Tian Shan, elucidating compressional tectonic processes.

Cite this article as Chen, Z., N. Fang, W. Xu, Y. Yao, P. Zhou, L. Xie, and L. Zhao (2025). Folding Growth Pattern of the Southern Tian Shan: Insights from the 2024 M_w 7.0 Wushi Earthquake and 2020 M_w 6.0 Jiashi Earthquake, Western China, *Seismol. Res. Lett.* **97**, 637–650, doi: 10.1785/0220250135.

Supplemental Material

Introduction

The deformation patterns by which intracontinental compressional orogens accommodate crustal shortening are critical for understanding intraplate tectonic deformation, earthquake generation, long-distance stress propagation, and mountain building processes (Molnar and Tapponnier, 1975; Tapponnier and Molnar, 1979; Avouac and Tapponnier, 1993; Yin *et al.*, 1998; Zhang *et al.*, 2004; Royden *et al.*, 2008). As a typical intracontinental compressional orogenic belt, the Tian Shan ("Shan" means "mountains" in Chinese) orogenic belt has undergone substantial crustal shortening and consequent mountain building due to far-field impact induced by the ongoing India-Eurasia collision (Fig. 1a) (Avouac *et al.*, 1993; Sobel and Dumitru, 1997; Yin *et al.*, 1998). On both flanks of the Tian Shan, a series of nearly east–west-trending foreland fold-and-thrust belts have developed as a result of north–south compressional forces (Avouac *et al.*, 1993; Sobel and Dumitru, 1997; Yin *et al.*, 1998; Allen *et al.*, 1999; Deng *et al.*, 2003). These belts are deemed to accommodate most of the crustal shortening across the Tian Shan (Yang, Li, and Wang, 2008; Wu *et al.*, 2023). However, the relative contributions of folding versus faulting in accommodating crustal shortening and driving mountain uplift in the Tian Shan remain controversial.

The Kepingtage fold-and-thrust belt (FTB) is a key active structure accommodating crustal shortening of the Tian Shan, formed during the propagation of the orogenic belt toward the Tarim basin (Fig. 1b,c). Previous studies suggest

1. School of Geosciences and Info-Physics, Central South University, Changsha, China, https://orcid.org/0000-0001-6015-3963 (ZC); https://orcid.org/0000-0001-6461-7219 (NF); https://orcid.org/0000-0001-7294-8229 (WX); https://orcid.org/0000-0003-0398-1476 (LX); 2. Urumqi Institute of Central Asia Earthquake, China Earthquake Administration, Urumqi, China

*Corresponding author: wenbin.xu@csu.edu.cn

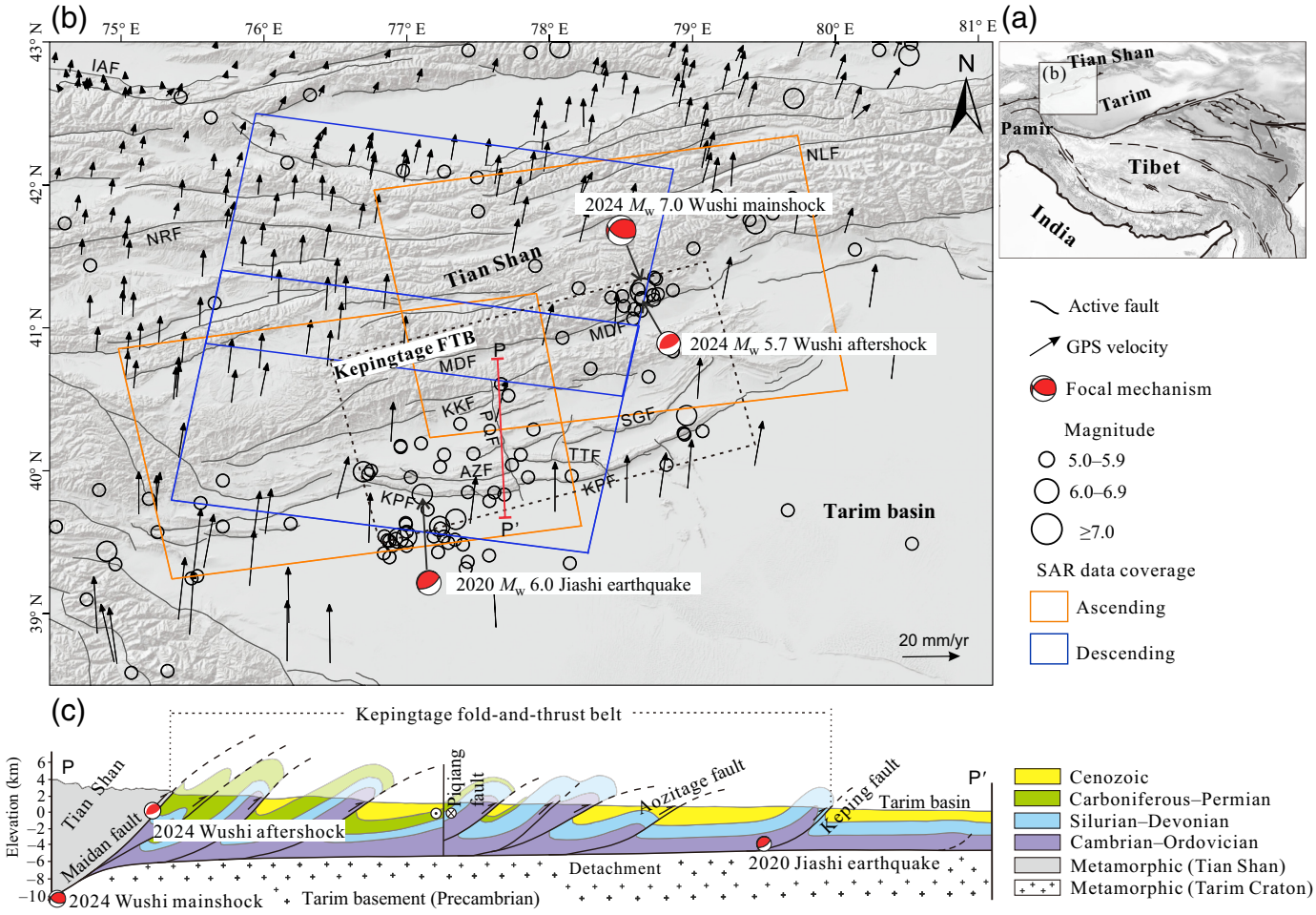

Figure 1. Seismotectonic framework of the study area. (a) Tectonic configuration of the India–Eurasia collisional system. (b) Active tectonics, Global Positioning System (GPS) velocity field and seismic activity in the southern Tian Shan. GPS velocities are relative to stable Eurasia and derived from Zheng *et al.* (2017). Focal mechanisms are from the U.S. Geological Survey (USGS). The hollow circles represent historical earthquakes with magnitudes 5+ since 1990, sourced from the USGS. The dashed rectangle marks the Kepingtage fold-and-thrust belt (FTB). The area of panel (b) is outlined by the white rectangle in panel (a). The gray curves denote the regional active faults, referenced from Deng *et al.* (2003) and Zelenin *et al.* (2022). AZF, Aozitage fault; IAF, Issyk-Ata fault; KKF, Kekebuke fault; KPF, Keping fault; NLF, Nalati fault; NRF, Naryn fault; MDF, Maidan fault; PQF, Piqiang fault; SGF, Saergantage fault; TTF, Tataiertage fault. (c) Cross-section P–P′ across the Kepingtage FTB showing the active structures and underlying rock layers (modified from Turner *et al.*, 2010), with the cross-section location depicted in panel (b). SAR, Synthetic Aperture Radar. The color version of this figure is available only in the electronic edition.

that crustal shortening is primarily absorbed by the piedmont fold-and-thrust belts (Yang, Deng, *et al.*, 2008; Zubovich *et al.*, 2010; Li *et al.*, 2021, 2022; Wu *et al.*, 2023). Geodetic observations show that the Kepingtage FTB absorbs a crustal shortening rate of 4–8 mm/yr, accounting for one-third of the total convergence across the western Tian Shan (Yang, Li, and Wang, 2008; Li *et al.*, 2022; Wu *et al.*, 2023). Structural analyses employing balanced cross sections and seismic reflection profiles consistently demonstrate that crustal shortening in these belts is accommodated through a combination of fault-related folding and reverse/thrust faulting (Allen *et al.*, 1999; Yang, Deng, *et al.*, 2008; Li *et al.*, 2018, 2023; Lü *et al.*, 2021), but which mechanism plays a more critical role in partitioning crustal shortening remains poorly understood.

Coseismic deformation investigations provide complementary tools for understanding tectonic deformation patterns because earthquake kinematics directly reflect the slip behavior of their causative faults and broader tectonic regimes. Two recent large earthquakes, namely the 2024 M_w 7.0 Wushi earthquake and the 2020 M_w 6.0 Jiashi earthquake (Fig. 1b), provide unique opportunities to elucidate folding or faulting contributions in absorbing crustal shortening in the Tian Shan, for these two events ruptured the root and front of the Kepingtage FTB, respectively (Fig. 1b,c). Between these two events lie a complex imbricate fold-and-thrust system that serves as a key region for revealing how the Tian Shan responds to crustal shortening.

Notably, the M_w 7.0 Wushi earthquake, on 23 January 2024, represents the first strong earthquake with magnitude 7+ in the southern Tian Shan over the past century (Fig. S1; Text S1, available in the supplemental material to this article) (Lü *et al.*, 2021; Zhao, Chen, *et al.*, 2024). The focal mechanisms from different organizations show that the 2024 Wushi earthquake is triggered by reverse motion with left-lateral strike-slip components (Table S1). Intriguingly, preliminary Interferometric Synthetic Aperture Radar (InSAR) observations indicate that the Wushi event caused notable surface uplift and subsidence but produced no clear surface ruptures, as evidenced by the smooth InSAR interference fringes and deformation fields (Zhao, Chen, *et al.*, 2024). However, subsequent investigations discovered an ~10-km-long surface rupture, with a maximum slip of ~0.4 m south of the epicenter (Qiu *et al.*, 2024; Zhang, Qian, *et al.*, 2024; Zheng *et al.*, 2024). Current interpretations suggest this rupture resulted not from the mainshock but from an M_w 5.7 aftershock a week later, on 30 January 2024 (Qiu *et al.*, 2024; Zheng *et al.*, 2024). Nevertheless, what factors led to the Wushi earthquake initially failing to produce surface ruptures but instead generating them during subsequent aftershock disturbances? This concern also makes the seismotectonic pattern of the southern Tian Shan subject to debate.

Here, we employ Differential Interferometric Synthetic Aperture Radar (D-InSAR) to derive the coseismic deformation fields of the 2024 Wushi and 2020 Jiashi earthquakes, respectively. A modified Bayesian nonlinear inversion method is utilized to constrain the geometry parameters and slip distributions of the causative fault (Zhao, Zhou, *et al.*, 2024). By integrating these results with regional geological data, we aim to clarify the seismogenic mechanisms and deformation patterns of the southern Tian Shan, providing new insights into tectonic deformation and mountain growth in compressional tectonic regimes.

Tectonic Background

The Tian Shan is a typical intracontinental orogenic belt rejuvenated during the late Cenozoic, extending ~2500 km long from east to west and 250–350 km wide from north to south in central Asia (Fig. S1) (Yin *et al.*, 1998; Xiao and Santosh, 2014; Wu *et al.*, 2023). This orogenic belt was initially formed by the subduction of the Paleo-Asian Ocean in the Paleozoic (Xiao *et al.*, 2020). The Cenozoic collision between Indian and Eurasian plates gave rise to the intense intracontinental deformation and orogeny in central Asia (Molnar and Tapponnier, 1975; Tapponnier and Molnar, 1979; Yin *et al.*, 1998; Deng *et al.*, 2003; Xiao and Santosh, 2014). Since the middle Miocene, north–south convergence between the Tian Shan and the Tarim basin has generated a series of nearly east–west-trending reverse faults within the Tian Shan and fold-and-thrust belts along its northern and southern frontal piedmonts (Text S2) (Yin *et al.*, 1998; Charreau *et al.*, 2009; Jia *et al.*, 2020). Global Positioning System (GPS) observations show the differential crustal shortening across the Tian Shan, with the shortening rates decreasing from west to east (Shen *et al.*, 2001; Wang *et al.*, 2001; Zubovich *et al.*, 2010; Zheng *et al.*, 2017; Li *et al.*, 2021; Wu *et al.*, 2023), showing ~20 mm/yr of north–south crustal shortening in the western Tian Shan and only 3–4 mm/yr in the eastern Tian Shan (Shen *et al.*, 2001; Zubovich *et al.*, 2010; Wu *et al.*, 2023).

The Kepingtage FTB along the southern Tian Shan front forms an imbricated thrust nappe structure, extending ~300 km from west to east and 60–140 km from north to south. This structure comprises five rows of east–west-trending thrust faults and fault-related anticlines (Fig. 1b) (Yang, Deng, *et al.*, 2008). These thrust faults converge to the same Precambrian basement detachment at a depth of 5–10 km (Fig. 1c) (Yin *et al.*, 1998; Allen *et al.*, 1999; Yang *et al.*, 2006; Yao *et al.*, 2020; Lü *et al.*, 2021). The Kepingtage FTB exhibits thin-skinned tectonic regimes near the frontal margin (closer to the basin) and thick-skinned regimes near the root zone (closer to the orogenic belt) (Allen *et al.*, 1999; Turner *et al.*, 2010). GPS measurements reveal a total shortening rate of 4.0 ± 1.5 mm/yr across the Kepingtage FTB, with higher rates in the east than in the west (Li *et al.*, 2022; Wu *et al.*, 2023). The inconsistency of shortening rates between the eastern and western parts is accommodated by the north-northwest-trending left-lateral Piqiang fault in the central Kepingtage FTB (Fig. 1b) (Yang *et al.*, 2006; Turner *et al.*, 2010, 2011).

The 2024 Wushi earthquake and the 2020 Jiashi earthquake ruptured the basin-mountain boundary fault (Maidan fault) and the frontal thrust fault (Keping fault) in the southern Tian Shan (Fig. 1b,c), respectively. The Maidan fault defines the topographic boundary between the Tian Shan and Tarim basin, extending more than 400 km in length (Fig. 1b), characterized by high-angle reverse slip with notable sinistral strike-slip components (Wu *et al.*, 2019; Zhao, Chen, *et al.*, 2024). This fault has been active since the late Quaternary and its long-term geological shortening rate is estimated to be 1–1.5 mm/yr (Wu *et al.*, 2019). The Keping fault, located at the southern front of the Kepingtage FTB, results from underthrusting of the Tarim basement beneath the Tian Shan orogenic belt (Fig. 1c) (Yin *et al.*, 1998; Allen *et al.*, 1999).

Data and Methods

Data and InSAR processing

InSAR technology has been widely utilized in monitoring surface deformation induced by earthquakes or tectonic activities based on the phase difference between radar signals reflected from the surface before and after tectonic events (Massonnet *et al.*, 1993; Bürgmann *et al.*, 2000; Fialko *et al.*, 2005; Meng *et al.*, 2024; Wang, Chang, *et al.*, 2024). This study collected pre- and post-earthquake Sentinel-1 ascending and descending radar images for the 2024 Wushi and 2020 Jiashi earthquakes (Table S2). The image data were downloaded from the Alaska Satellite Facility Data Search (see Data and Resources). We

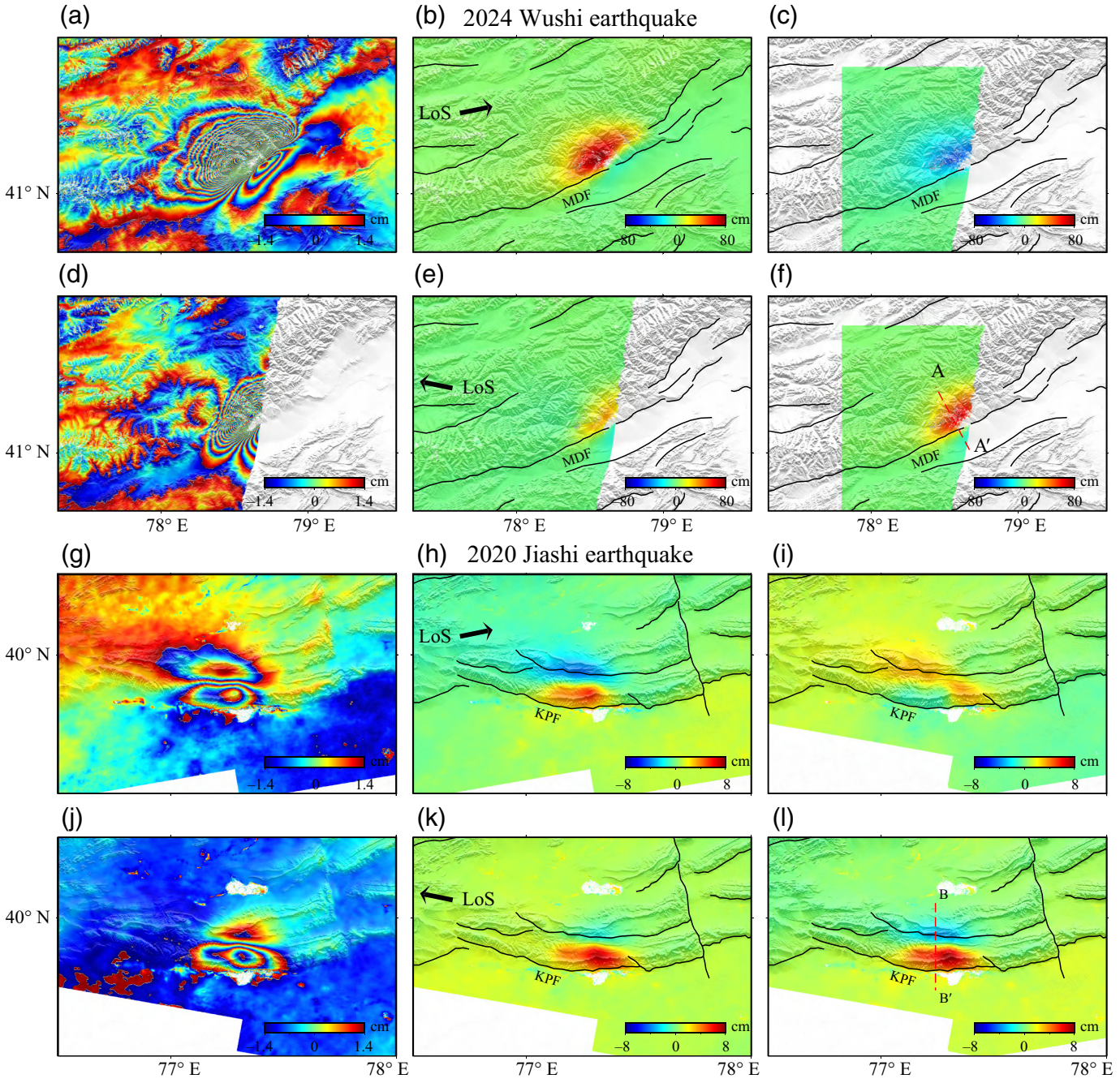

employed the software GAMMA to conduct D-InSAR processing. The interferograms are multilooked with a ratio of 10 : 2 (i.e., range : azimuth) to improve the signal-to-noise ratio. The 30 m resolution digital elevation model was utilized to simulate and correct the topographic phase. The interferograms were processed using the adaptive filtering algorithm and subsequently unwrapped via the minimum cost flow method (Goldstein and Werner, 1998). Long-wavelength atmospheric delays and orbital errors were removed through polynomial fitting (Fournier *et al.*, 2011; Xu *et al.*, 2018). Finally, we utilized SAR satellite parameters to transform the Synthetic Aperture Radar (SAR) coordinate into the geographical coordinate system and obtain the coseismic deformation fields (Fig. 2).

Figure 2. Interferometric Synthetic Aperture Radar (InSAR) coseismic deformation fields for the 2024 Wushi and 2020 Jiashi earthquakes. (a,b) The ascending and descending track interferograms of the 2024 Wushi earthquake. (c,d) The line-of-sight (LoS) deformation fields for the ascending and descending tracks of the Wushi earthquake. (e,f) The east–west deformation field and the vertical deformation field of the Wushi earthquake. (g–l) are similar to (a–f), but for the 2020 Jiashi earthquake. KPF, Keping fault; MDF, Maidan fault. The color version of this figure is available only in the electronic edition.

Given that the 2024 Wushi and 2020 Jiashi earthquakes are dominated by reverse or thrust motion, vertical deformation more accurately delineates their deformation features. We

further decomposed the line-of-sight (LoS) deformation fields into vertical and horizontal deformation components. Currently, most SAR satellites employ near-polar orbits and right-looking imaging modes, resulting in variations in the accuracy of InSAR deformation monitoring in different directions, particularly rendering it insensitive to deformation in the north–south direction. Therefore, we extracted the east–west and vertical deformation components while neglecting the north–south displacement (Fig. 2). By integrating the ascending and descending LoS deformation fields, we calculated the east–west and vertical deformation fields based on the following geometric relationship:

$$\begin{bmatrix} D_{\mathrm{LOS}(AT)} \\ D_{\mathrm{LOS}(DT)} \end{bmatrix} = \begin{bmatrix} -\sin\theta\cos\alpha, \cos\theta \\ -\sin\theta\cos\alpha, \cos\theta \end{bmatrix} \begin{bmatrix} D_E \\ D_U \end{bmatrix}. \quad (1)$$

In equation (1), $D_{\mathrm{LOS}(AT)}$ and $D_{\mathrm{LOS}(DT)}$ represent the LoS deformation in the ascending and descending track directions, respectively. θ is the incidence angle, and α is the azimuth angle. D_E and D_U represent the east-west and vertical deformation components.

Inversion of fault geometry and slip distribution

The geometry parameters and slip distributions of the causative fault inverted from InSAR-derived surface deformation can reveal the fault kinematics, offering insights into the seismogenic mechanisms and energy release (Massonnet *et al.*, 1993; Goldstein and Werner, 1998; Jónsson *et al.*, 2002; Fukuda and Johnson, 2010; Wang, Chang, *et al.*, 2024). In this study, we employ a modified Bayesian approach (MF-J method) to simultaneously invert for fault geometry parameters and slip distributions using Okada solutions for rectangular dislocations in a homogeneous, elastic half-space, assuming a Poisson's ratio of 0.25 and a shear modulus of 30 GPa (Text S3) (Okada, 1985; Zhao, Zhou, *et al.*, 2024). First, the MF-J method assigns initial values following a uniform distribution for the nonlinear parameters and estimates the initial linear slip distribution and hyperparameters through the variance component estimation (VCE) method (Fan *et al.*, 2017). The nonlinear parameters include *Ex*, *Ey*, *Ez* (coordinates of the fault's upper left corner) as well as strike and dip angles. The two hyperparameters (Sig_d and Sig_a) represent the variance components of the actual and virtual observations, respectively (Text S3; Figs. S2 and S5). Second, the MF-J method calculates the corresponding posterior probability density function (PDF) using the equations from Fukuda and Johnson (2010). Third, the MF-J method perturbs the current parameter set by adding a random step (with step size scaled by a uniform random number) to generate a new candidate set of nonlinear parameters and hyperparameters. The new parameter set is used to invert the slip distribution with the VCE method, and then the new full posterior PDF is recalculated. Finally, the MF-J method determines the likelihood ratio R between the new PDF and the previous PDF and accepts the new group of linear and nonlinear parameters if $\min\{R,1\}$ exceeds a random value following a uniform distribution from 0 to 1 based on the Metropolis algorithm (Metropolis *et al.*, 1953). After sufficient iterations, the sampling results of the parameters are obtained. Initial samples (generally the first few thousand iterations) are discarded as the burn-in period until convergence is achieved. Then, we extract the stabilized samples after the burn-in period (Text S3).

To enhance the computational efficiency of the inversion process, we apply the quadtree sampling method for data set downsampling (Jónsson *et al.*, 2002). This method uses the deformation gradient as the indicator to allow dense sampling in the areas with large deformation gradients but coarse sampling in areas with small changes, which is suitable for coseismic deformation data reduction (Gao *et al.*, 2022). We obtain 956 and 789 data points for the 2024 Wushi ascending and descending deformation fields (Fig. S4). Based on the empirical relationship between the fault size and moment magnitude (Wells and Coppersmith, 1994), we set the fault length and width to 60 and 40 km, to allow an exhaustive search in the potential space. We discretize the fault plane into 600 patches with a size of 2 km × 2 km (Fig. 3). Then, we use the coordinates (78.649° E, 41.269° N) as a reference point to convert the fault's geographic coordinates into UTM coordinates. The initial values and bounds for the fault's geometric parameters are presented in Table S3. We constrain the fault strike between 200° and 300° and limit the fault dip between 1° and 60° based on previous studies (Qiu *et al.*, 2024; Zhao, Chen, *et al.*, 2024; Zheng *et al.*, 2024). We then execute the MF-J method for 15,000 iterations, considering the first 10,000 iterations as the burn-in period. After the burn-in period, we retain the fault geometric parameters, hyperparameters, and slip distribution every 25 iterations to ensure sample independence. Finally, we resolve the average and standard deviation of each parameter (Figs. S2 and S3; Table S3).

For the 2020 Jiashi earthquake, we acquire 523 and 530 data points for the ascending and descending deformation fields, respectively (Fig. S7). We set the fault dimensions of 40 km × 20 km for exhaustive parameter space exploration. The fault plane is discretized into 200 patches with a size of 2 km × 2 km (Fig. 4). Using the coordinates (77.27° E, 39.89° N) as the reference point, we transform the geographic coordinates to UTM. Initial values and bounds are listed in Table S4. The strike and dip angles are constrained to 200°–360° and 5°–30° based on previous studies (Yao *et al.*, 2020; Wu *et al.*, 2024). The MF-J inversion is conducted for 10,000 iterations (with 5,000 as burn-in), with parameters sampled every 25 iterations. Then, we calculate the average and standard deviation of each parameter (Figs. S5 and S6; Table S4). The program code for this inversion method and the processing results for the 2024 Wushi and 2020 Jiashi earthquakes are accessible on the GitHub platform (see Data and Resources).

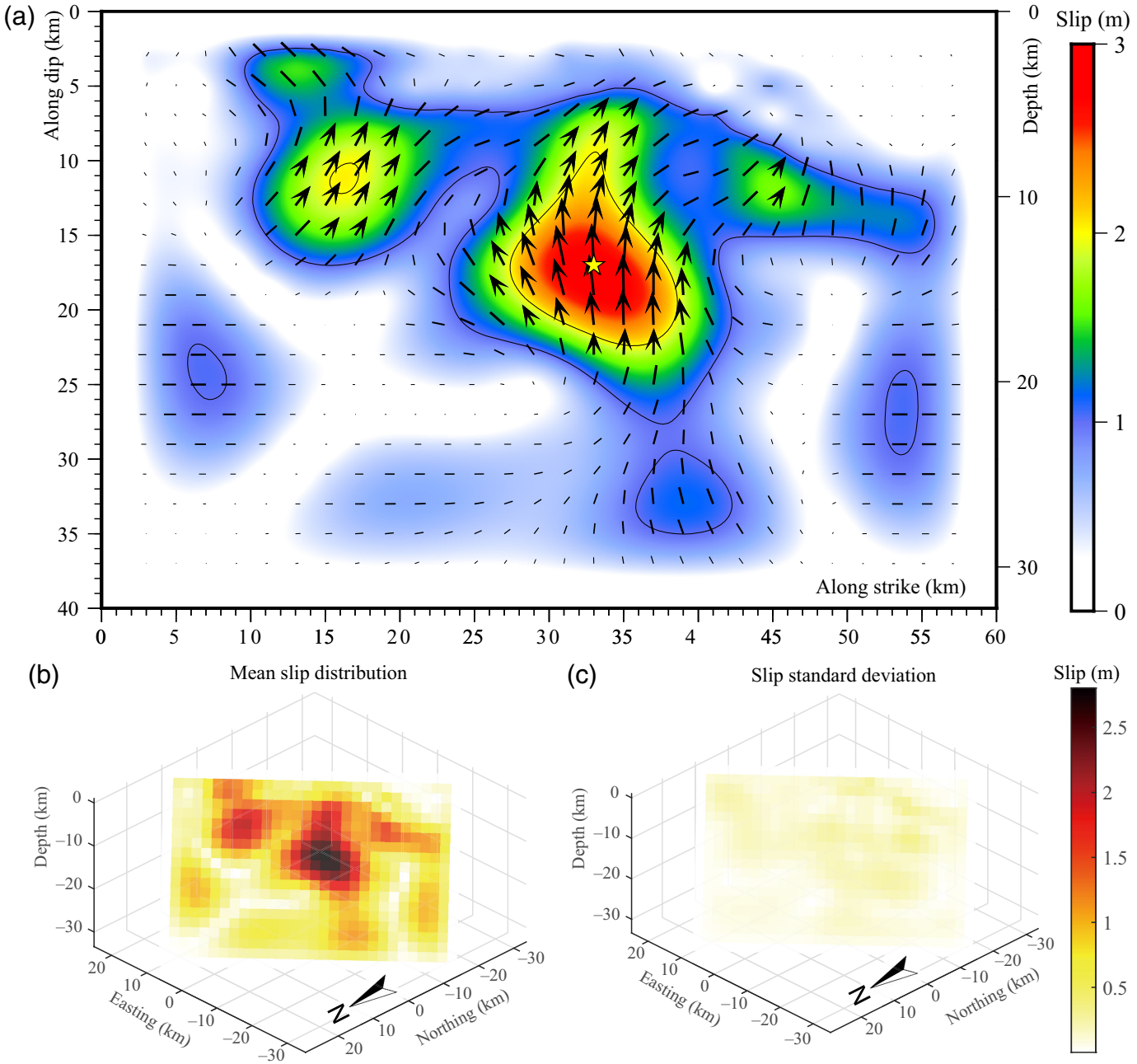

Figure 3. Slip distributions and slip standard deviation of the 2024 Wushi earthquake. (a) 2D slip distribution of the 2024 Wushi earthquake showing slip magnitudes and orientations. (b,c) 3D slip distribution and slip standard deviation (uncertainty) of the Wushi earthquake. The color version of this figure is available only in the electronic edition.

Results

Coseismic deformation fields and slip kinematics of the 2024 Wushi earthquake

The interferograms derived from ascending and descending tracks reveal two distinct elliptical deformation zones separated by the Maidan fault (Fig. 2a,b). The northern deformation zone exhibits significantly greater spatial extent and magnitude compared to the southern zone. The deformation ellipses are oriented along the east-northeast–west-southwest direction, consistent with both the focal mechanism solutions (Table S1) and the strike of the Maidan fault.

Both ascending and descending LoS deformation fields display similar deformation patterns (Fig. 2c,d), indicating dominant vertical motion induced by the Wushi earthquake. The northern side of the Maidan fault experienced uplift, while the southern side underwent subsidence. Specifically, the ascending track measured ~0.77 m uplift and ~0.10 m subsidence, whereas the descending track detected ~0.38 m uplift and ~0.14 m subsidence (Fig. 2c,d). The continuous fringe patterns in both interferograms suggest no surface rupture occurred during the earthquake (Fig. 2a,b). However, the denser interference

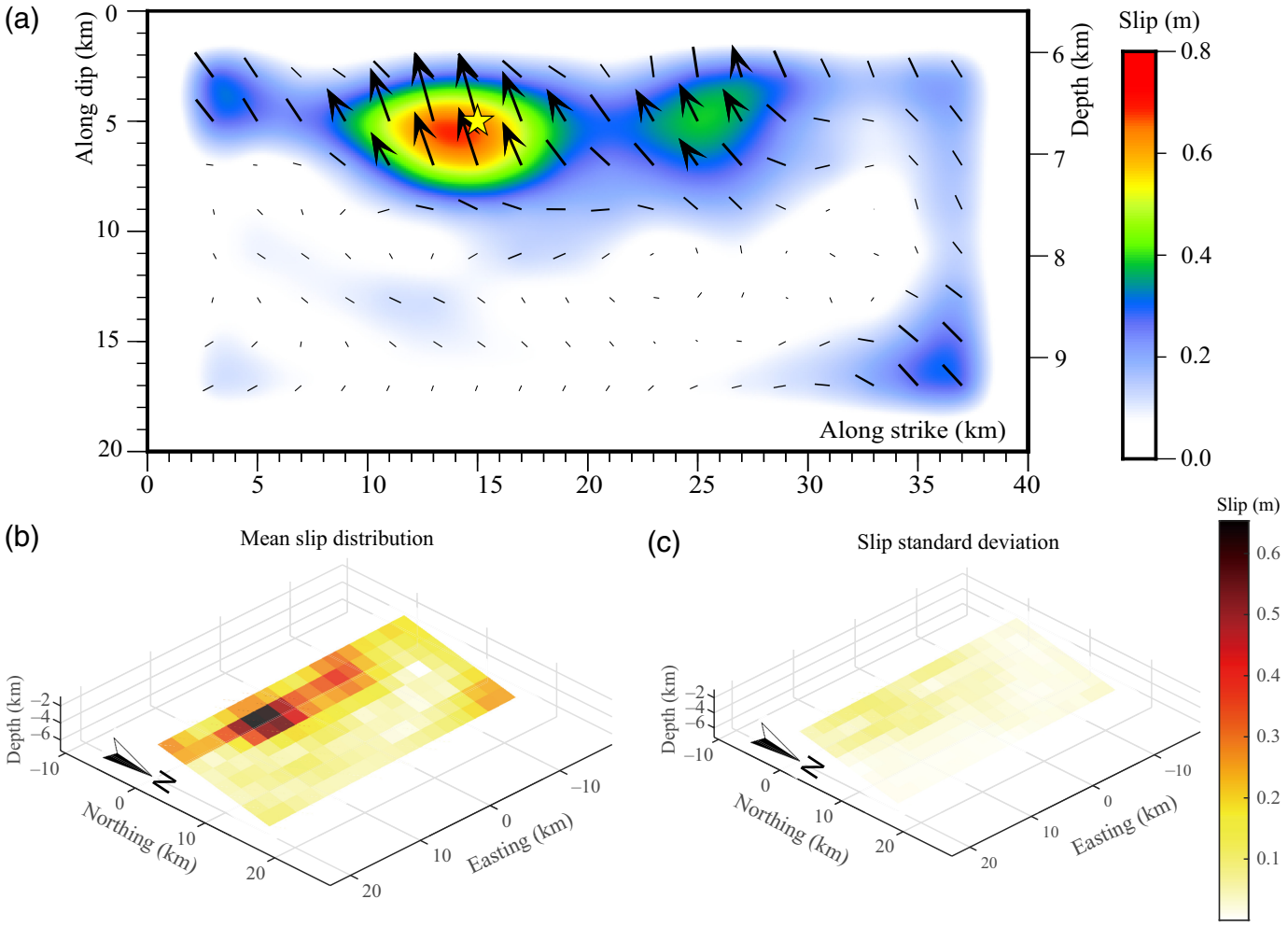

Figure 4. Slip distributions and slip standard deviation of the 2020 Jiashi earthquake. (a) 2D slip distribution of the 2020 Jiashi earthquake showing slip magnitudes and orientations. (b,c) 3D slip distribution and slip standard deviation (uncertainty) of the Jiashi earthquake. The color version of this figure is available only in the electronic edition.

fringes near the Maidan fault indicate a steep deformation gradient along the causative fault (Fig. 2a,b).

The east–west and vertical deformation fields further demonstrate that the Wushi earthquake is a primarily reverse-faulting event with a significant left-lateral component (Fig. 2e,f). The east–west deformation field indicates westward motion of the northern block relative to the southern block, with a left-lateral displacement of ~0.5 m (Fig. 2e). The vertical displacement field reveals that the hanging wall (northern block) was uplifted by a maximum of ~0.68 m relative to the footwall (southern block), which subsided by ~0.12 m, yielding a total vertical displacement of ~0.8 m (Fig. 2f). The transition between uplift and subsidence spatially coincides with the surface traces of the Maidan fault.

The Bayesian inversion yields a strike angle of 227.5° ± 0.6° and a dip angle of 53.7° ± 0.7°, dipping to northwest (Figs. S2 and S3). The slip distribution confirms that the earthquake is dominated by reverse faulting with a notable left-lateral component (Fig. 3a). The maximum slip amount is ~2.8 m at a depth of ~15 km below the surface (Fig. 3a). The seismic moment released by the rupture is 4.09×10^{19} N · m, equivalent to a moment magnitude M_w 7.0. The root mean square error (RMSE) between the predicted values based on the slip distribution model and the observed values are ~1.3 cm (Fig. S4).

Coseismic deformation fields and slip kinematics of the 2020 Jiashi earthquake

The interferograms from InSAR ascending and descending tracks, coupled with the LoS deformation fields, also identify two elliptical deformation zones induced by the 2020 Jiashi earthquake (Fig. 2g,h). The long axis of these ellipses align nearly east–west, consistent with the strike of the Kepingtage FTB. Although the ascending track reveals a near-symmetrical distribution of the two deformation ellipses (Fig. 2g), the descending track shows a larger southern ellipse compared to the northern one (Fig. 2h).

Unlike typical earthquakes where the causative fault lies at the intersection of deformation zones, the Jiashi earthquake

exhibits an anomalous deformation pattern: the intersection of uplift and subsidence does not coincide with the Keping fault's traces. Instead, the fault traces are distributed along the southern margin of the entire deformation field, with the vast majority of the deformed area being confined to its hanging wall (Fig. 2i–l). Localized decoherence is observed along the fault traces (Fig. 2g,h), indicating small surface displacements along the Keping fault. Both ascending and descending LoS deformation fields consistently indicate vertical-dominated motion, characterized by uplift in the southern ellipse and subsidence in the northern ellipse (Fig. 2i,j). The interferograms and deformation fields demonstrate nearly continuous uplift and subsidence variation.

The east–west and vertical deformation fields show a pure thrust motion (Fig. 2k,l). The maximum uplift is measured to be ∼0.07 m, whereas the maximum subsidence is ∼0.03 m, yielding a total vertical displacement of ∼0.1 m (Fig. 2l). The east–west deformation field exhibits a diffuse movement from the uplift center toward the edges, with the eastern part moving eastward and the western part westward (Fig. 2k).

The Bayesian inversion resolves a strike angle of 276° ± 1.4° and a dip angle of 12.5° ± 1.0°, dipping to north (Figs. S5 and S6). The slip distribution model further supports dominant thrust motion, with minor right-lateral strike-slip components (Fig. 4a). The maximum slip amount is ∼0.65 m, located at a depth of ∼6.8 km below the surface (Fig. 4a). The released seismic moment is 2.32×10^{18} N · m, equivalent to a moment magnitude $M_w \sim 6.18$. The RMSE between the predicted values and the observed values is ∼0.43 cm (Fig. S7).

Discussion

Deformation patterns and seismogenic mechanisms of the 2024 Wushi and 2020 Jiashi earthquakes

The InSAR interferograms and the cross-fault deformation profiles reveal that the surface deformation caused by the 2024 Wushi earthquake exhibits good spatial continuity (Fig. 2a,b and 5a), indicating that this event did not rupture the surface (Ding *et al.*, 2024; Qiu *et al.*, 2024; Zhao, Chen, *et al.*, 2024; Zheng *et al.*, 2024). Notably, the interference fringe density and deformation gradient of the Wushi earthquake peak near the causative fault (Figs. 2a,b and 5a). For the 2020 Jiashi earthquake, the deformation gradient reaches its maxima within 5–10 km north of the causative fault (Fig. 5b), and localized subsidence was observed along the southern margin of the Keping fault, with a width not exceeding 2 km, which has been rarely reported in previous studies (Fig. 5b) (Yao *et al.*, 2020; He *et al.*, 2021; Wang *et al.*, 2022; Zhang *et al.*, 2023; Wu *et al.*, 2024). Although minor localized subsidence occurred, the Jiashi earthquake generally exhibits nearly continuous surface deformation (Fig. 5b).

The spatially continuous deformation fields of the Wushi and Jiashi earthquakes are interpreted as surface folding resulting from deep reverse/thrust faulting. Folding deformation generally refers to the bending or warping of layered rock strata under tectonic forces, leading to the formation of curved or wavelike surface structures (Suppe, 1983), which are often associated with distributed, off-fault inelastic deformation within the bulk crust. It is critical to acknowledge that our inversion model, which is based on dislocations in a purely elastic half-space (see the Data and Methods section), is by design only capable of inferring the geometry and slip of the underlying fault (Okada, 1985; Zhao, Zhou, *et al.*, 2024). Therefore, this model cannot directly quantify any potential contribution of distributed inelastic deformation to the observed surface folding deformation. Accordingly, we clarify that our interpretation of the term "folding" here refers primarily to the geomorphic expression and the kinematic pattern of deformation, rather than to a specific mechanical mechanism involving inelastic deformation.

The folding pattern of the Wushi earthquake shows an anticline feature, with an asymmetrical anticline on the hanging wall of the Maidan fault, featuring a gentle deformation gradient on the northern limb and a steep gradient on the southern limb (Fig. 5a). Conversely, the Jiashi earthquake displays a combination of anticline and syncline, with an anticline near the fault and a syncline more than 8 km away from it (Fig. 5b). The difference in fold styles between these two events may be attributed to the different dip angles of the causative faults. Fault geometry derived in this study suggests that the Wushi earthquake was triggered by a high-angle reverse fault with a dip angle of 53.7°, whereas the fault plane of the Jiashi earthquake exhibits a much gentler dip angle of only 12.5° (Table S1). Besides, the slip distribution of the Wushi fault shows an upward gradual reduction of slip along the fault plane, together with its asymmetric deformation gradient (a steeper forelimb and a gentler backlimb), indicating that the Wushi event conforms to the fault-propagation fold pattern (Fig. 5a) (Suppe, 1983; Yang *et al.*, 2006; Jabbour *et al.*, 2012). In contrast, the Jiashi earthquake slip core is concentrated at 6–7 km depth, consistent with the local detachment depth (Yin *et al.*, 1998; Allen *et al.*, 1999; Yang *et al.*, 2006). Therefore, the Jiashi event demonstrates a low-angle thrusting along the deep detachment surface, corresponding to the detachment fold pattern (Fig. 5b). However, unlike the symmetrical arch observed in typical detachment folds (Yang *et al.*, 2006; Contreras, 2010), the Jiashi earthquake displays a wavelike anticline–syncline complexity (Fig. 5b).

Seismic reflection profiles reveal the gradually evolving crustal structure in the southern Tian Shan (Lü *et al.*, 2021). The cover thickness of the Kepingtage FTB is ∼5 km at its front edge and gradually increases northward to about 8 km at its root (Allen *et al.*, 1999; Yang *et al.*, 2006; Lü *et al.*, 2021). The fault-slip distribution inverted in this study shows that the focal depth of the Wushi earthquake reaches up to ∼15 km, far exceeding the cover thickness. Consequently, the Wushi earthquake

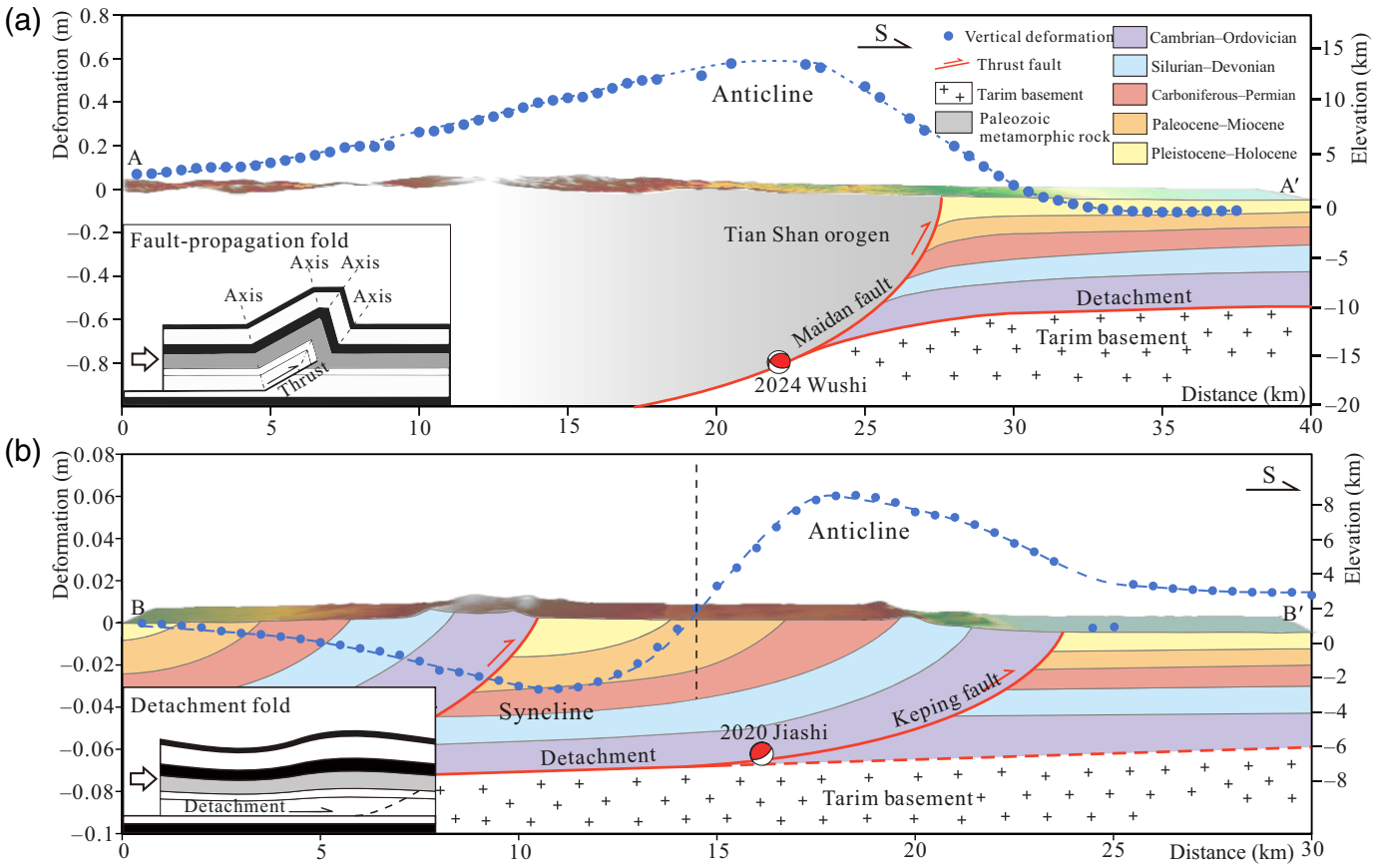

Figure 5. Deformation cross sections of the 2024 Wushi and 2020 Jiashi earthquakes. (a) Cross-section A–A′ showing the vertical deformation of the 2024 Wushi earthquake, topographic relief, active structures, and underlying rock layers, with the inset of the fault-propagation fold model (modified from Yang *et al.*, 2006). The cross-section location is depicted by the red-dashed line in Figure 2f. (b) Cross-section B–B′ showing the vertical deformation of the 2020 Jiashi earthquake, topographic relief, active structures, and underlying rock layers, with the inset of the detachment fold model. The cross-section location is depicted by the red-dashed line in Figure 2l. The color version of this figure is available only in the electronic edition.

simultaneously ruptured the Paleozoic metamorphic rocks of the Tian Shan orogen and the Precambrian crystalline basement of the Tarim basin (Fig. 5a). Given that the Tarim basement rocks have significantly greater strength than the sedimentary rocks in the overlying cover (Allen *et al.*, 1999; Yang *et al.*, 2006), the Maidan fault is more capable of accumulating strain compared to the Keping fault, thus generating larger magnitude earthquakes.

In addition, the Maidan fault is the basin–mountain boundary fault between the Tarim Craton and the Tian Shan orogen, exhibiting better geometry linearity and a higher degree of fault maturity (Wu *et al.*, 2019), making it prone to triggering longer ruptures. In contrast, thrust faults at the front of the Kepingtage FTB are intersected by multiple northwest-trending strike-slip faults, resulting in discontinuous fault geometry (Li *et al.*, 2019; Lü *et al.*, 2021; Wu *et al.*, 2024), thus limiting the rupture propagation and potentially explaining why the moderate-magnitude earthquakes such as the Jiashi earthquake are frequently observed in the Kepingtage FTB.

Surface rupture mechanism of the 2024 Wushi earthquake

A surface rupture was identified ~15 km south of the 2024 Wushi epicenter, stretching ~10 km in length and featuring a maximum vertical displacement of ~0.4 m (Qiu *et al.*, 2024; Zheng *et al.*, 2024; Zhang, Qian, *et al.*, 2024). Intriguingly, the surface rupture is characterized by a south-dipping reverse faulting, in contrast to the north-dipping mechanism of the Wushi mainshock (Zhang, Qian, *et al.*, 2024).

To ascertain whether the surface rupture was caused by the aftershock or mainshock, we re-extracted InSAR surface deformation fields, encompassing the M_w 5.7 aftershock solely (Fig. 6). Both ascending and descending deformation fields detected an ~10-km-long surface rupture (R1) on the northern side of the Maidan fault in the aftershock deformation fields (Fig. 6d,e), striking to the east-northeast direction, with a maximum displacement of ~0.5 m (Fig. 6f). The southern part of the rupture (R1) exhibits uplift relative to the northern part (Fig. 6d,e), contrasting with the mainshock deformation pattern (Fig. 6a,b), but consistent with the field observations (Zhang, Qian, *et al.*, 2024). The fault geometry inversion reveals that

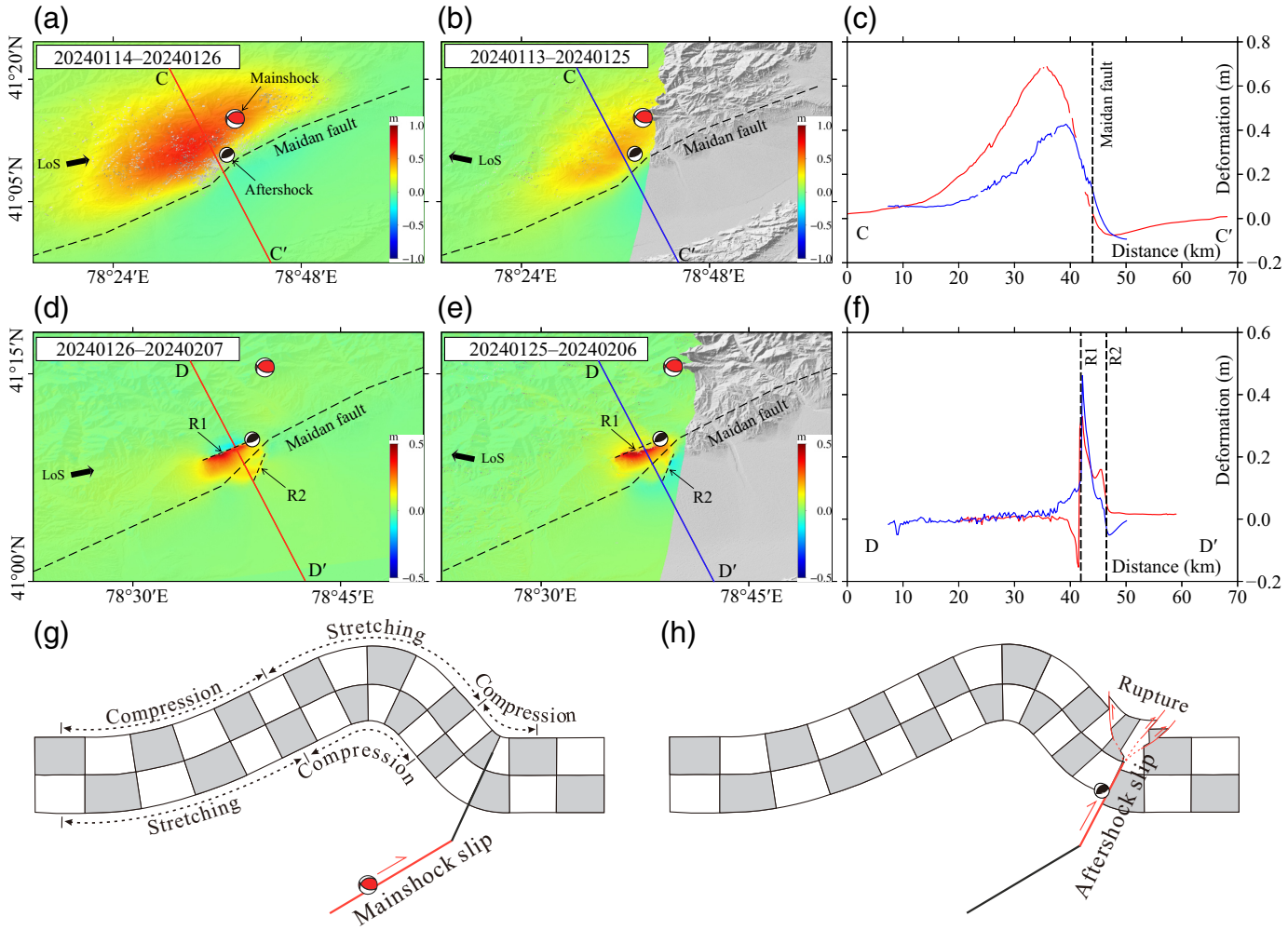

Figure 6. InSAR deformation fields and deformation profiles of the M_w 7.0 Wushi mainshock and the M_w 5.7 Wushi aftershock. Panels (a–c) represent the ascending deformation field, descending deformation field, and deformation profile C–C′ of the M_w 7.0 Wushi mainshock. Profile C–C′ locations are marked by red and blue lines in panels (a) and (b). (d–f) represent the ascending deformation field, descending deformation field, and deformation profile D–D′ of the M_w 5.7 Wushi aftershock, showing two surface ruptures (R1 and R2). Profile D–D′ locations are outlined by red and blue lines in panels (d) and (e). (g) Schematic diagram showing the shallow fold deformation induced by deep mainshock slip. (h) Schematic diagram showing surface positive flowerlike ruptures generated by shallow aftershock slip (modified from Zhang, Li, *et al.*, 2024). Focal mechanisms are from the USGS. The color version of this figure is available only in the electronic edition.

the aftershock rupture exhibits a strike of ~60°, dipping to the southeast, contrary to the mainshock mechanism (Qiu *et al.*, 2024; Zheng *et al.*, 2024; Famiglietti *et al.*, 2025). Some studies have attributed this rupture to the broad temporal span of InSAR observations, which may capture additional deformation resulting from aftershocks (Qiu *et al.*, 2024; Zheng *et al.*, 2024). However, the field survey conducted one day prior to the M_w 5.7 aftershock failed to observe the surface rupture, but immediately discovered it in the afternoon of the day that the M_w 5.7 aftershock occurred (Zhang, Qian, *et al.*, 2024), suggesting that this rupture was primarily induced by the M_w 5.7 aftershock. In addition, the aftershock deformation fields detected another minor surface rupture (R2) on the southern side of the Maidan fault (Fig. 6d,e), with a displacement of ~0.15 m (Fig. 6f). This rupture dips to the northwest, consistent with the mainshock mechanism (Qiu *et al.*, 2024).

The inverted fault-slip distribution reveals that the mainshock slip concentrated at depths exceeding 5 km below the surface, peaking at around 15 km, whereas the aftershock slip occurred in the shallow crust above 5 km and propagated to the surface (Fig. S8) (Qiu *et al.*, 2024; Zheng *et al.*, 2024). The nonpropagation of the mainshock slip to the surface could be attributed to variations in fault geometry, particularly the increasing dip angles toward the surface along the Maidan fault (Fig. 1c) (Zhang *et al.*, 2019; Lü *et al.*, 2021). Variations in dip angles along the fault plane prevent the mainshock rupture from propagating to the surface, while causing a slip deficit and Coulomb stress loading in the shallow crust (Fig. S8).

Therefore, we propose a two-stage model to explain the surface ruptures during the 2024 Wushi event (Fig. 6g,h):

First, the mainshock slip concentrated below 5 km caused shallow fold deformation without notable surface ruptures, but formed a compressive strain zone at the leading tip of the fold (Fig. 6g), generating a slip deficit zone in the shallow crust (Fig. S8a,c); second, the aftershock slip occurring above 5 km compensated for the shallow slip deficit, leading to positive flowerlike ruptures in the folded strain zone (Fig. 6h, Fig. S8b,d). This model explains why the aftershock rupture exhibits an opposite dip direction compared to the mainshock mechanism. In addition, because the aftershock ruptures were superimposed on the mainshock deformation fold, a portion of the compressive strain accumulated in the fold was released through surface rupturing, resulting in the actual displacement magnitude (~0.5 m) of the aftershock being larger than the seismically calculated magnitude (M_w 5.7) based on magnitude–displacement scaling relationships (Wells and Coppersmith, 1994).

Implications for seismicity and growth patterns of the southern Tian Shan

GPS measurements suggest that crustal shortening in the Tian Shan orogenic belt is predominantly absorbed by the foreland fold-and-thrust belts (Deng *et al.*, 2003; Yang, Li, and Wang, 2008). However, the 2024 Wushi earthquake and recent GPS/InSAR observations demonstrate that a portion of convergence strain is also absorbed within the Tian Shan interior (Li *et al.*, 2021; Lü *et al.*, 2021; Wu *et al.*, 2023; Wang, Xu, *et al.*, 2024). In spite of the limited crustal shortening rates within the Tian Shan, the high-angle reverse faults within the orogenic interior still have capacity to produce considerable strain accumulation and cause large-magnitude earthquakes. This seismic hazard potential arises because, under equivalent crustal shortening conditions, steeper-dipping reverse faults accumulate greater elastic strain than their gentler counterparts. In addition, recent geodetic studies have mapped the spatial distribution of interseismic coupling of the Maidan fault before the 2024 Wushi event and identified four locked segments with high seismic risks (Wang, Xu, *et al.*, 2024). However, although the Wushi earthquake ruptured only one of these segments, the remaining three segments retain the potential to generate M 7+ earthquakes.

Fault-bend folds triggered by seismic events may exhibit either elastic or inelastic deformation characteristics (Mallick *et al.*, 2021). Geophysical modeling suggests that distinguishing between the elastic and inelastic responses to fault slip is possible only during the postseismic period following large earthquakes (Mallick *et al.*, 2021). In the case of the Wushi event, the shallow fold induced by deep coseismic slip underwent partial postseismic recovery, manifested as surface ruptures in the shallow slip deficit zone (Fig. 6). Nevertheless, the surface deformation caused by the Wushi event remains characterized by folding deformation because the postseismic recovery produced only ~10-km-long surface ruptures, significantly shorter than the ~50-km-long coseismic deformation field (Fig. 6). Moreover, geodetic observations reveal that fault-bend folding develops not only during long-lasting postseismic phases (Zhou *et al.*, 2016), interseismic periods (Chong *et al.*, 2024), and aseismic slip episodes (Tsukahara and Takada, 2018), but also during instantaneous coseismic phases (Yao *et al.*, 2020; Qiu *et al.*, 2024), as observed in the 2024 Wushi and 2020 Jiashi events.

Both thrust/reverse faulting and folding contribute to mountain growth and outward expansion of compressional orogenic belts. The southern Tian Shan foreland hosts multiple imbricated fold-and-thrust belts that accommodate regional crustal shortening primarily through low-angle detachment folding along a uniform décollement (Yin *et al.*, 1998; Allen *et al.*, 1999; Yang *et al.*, 2006; Turner *et al.*, 2010; Tian *et al.*, 2016; Lü *et al.*, 2021). Recent paleoseismic investigations have identified multiple fold earthquakes within the southern Tian Shan (Zhang, Li, *et al.*, 2024). In this study, although localized surface ruptures were observed in the deformation fields, the Wushi and Jiashi events remain characterized as fold-dominated deformation features. Thus, we suggest that folding deformation plays a predominant role in accommodating crustal shortening in the southern Tian Shan, which is of great significance for understanding deformation patterns and mountain growth processes in intracontinental compressive orogenic belts.

Conclusion

The two powerful earthquakes that occurred in the southern Tian Shan, the 2024 M_w 7.0 Wushi earthquake and the 2020 M_w 6.0 Jiashi earthquake, provide critical cases for understanding tectonic deformation patterns in compressive tectonic regimes. This study employed Sentinel-1 radar images provided by the European Space Agency to capture the coseismic deformation fields of both events and then applied a modified Bayesian inversion method to derive the geometry parameters and the slip distributions along the fault planes. Our findings reveal that both Wushi and Jiashi earthquakes exhibit shallow fold deformation caused by deep reverse/thrust faulting. The high-angle reverse motion of the Wushi earthquake produced a fault-propagation fold in the shallow crust (<5 km depth), whereas the low-angle thrusting along detachment during the Jiashi earthquake generated a detachment fold within the sedimentary cover layer. The surface ruptures observed in the Wushi event resulted from positive flowerlike structures produced by the subsequent M_w 5.7 aftershock, explaining the opposite dip direction between the aftershock and mainshock mechanisms. The deformation patterns of the two earthquakes highlight the dominance of folding deformation in accommodating shallow crustal shortening in the southern Tian Shan.

Data and Resources

The Synthetic Aperture Radar (SAR) data used in this study was provided by the European Space Agency (ESA) through the ASF Data Hub website (https://search.asf.alaska.edu/). The earthquake focal mechanisms were obtained from the U.S. Geological Survey (USGS; https://earthquake.usgs.gov), Global Centroid Moment Tensor (Global CMT; https://www.globalcmt.org), China Earthquake Networks Centre (CENC; https://news.ceic.ac.cn/) and National Earthquake Data Center (NEDC; https://data.earthquake.cn/). The program code of the MF-J inversion method and the processing results for the 2024 Wushi and 2020 Jiashi earthquakes are accessible on the Github platform (https://github.com/XiongZhao0303/MF-J-method-to-simultaneously-solve-for-the-co-seismic-fault-geometry-and-slip-parameters/blob/main/MF-J/readme.txt). Some figures were drawn by Generic Mapping Tools (GMT; Wessel *et al.*, 2019). All websites were last accessed in January 2025. The supplemental material includes Text S1–S3, Figures S1–S8, and Tables S1–S4.

Declaration of Competing Interests

The authors acknowledge that there are no conflicts of interest recorded.

Acknowledgments

The authors are grateful to Zhao Xiong from Wuhan University for providing the MF-J inversion program code. The authors thank Rebetsky Y. L. from Institute of Physics of the Earth, Russian Academy of Science, for sharing the regional historical seismic data. This research was supported by National Natural Science Foundation of China (42174023, 42304037), Natural Science Foundation of Hunan Province (2024JJ3031), and Frontier Cross Research Project of Central South University (2023QYJC006). The authors sincerely thank Editor-in-Chief Allison Bent and the two anonymous reviewers for their constructive comments, which have significantly improved the quality of this work.

References

Allen, M. B., B. F. Windley, C. Zhang, Z. Y. Zhao, and H. R. Wang (1999). Late Cenozoic tectonics of the Kepingtage thrust zone: Interactions of the Tien Shan and Tarim, *Tectonics* **18,** no. 4, 639–654, doi: 10.1029/1999TC900019.

Avouac, J.-P., and P. Tapponnier (1993). Kinematic model of active deformation in central Asia, *Geophys. Res. Lett.* **20,** no. 10, 895–898, doi: 10.1029/93GL00128.

Avouac, J.-P., P. Tapponnier, M. Bai, H. You, and G. Wang (1993). Active thrusting and folding along the northern Tien Shan and Late Cenozoic rotation of the Tarim relative to Dzungaria and Kazakhstan, *J. Geophys. Res.* **98,** no. B4, 6755–6804, doi: 10.1029/92JB01963.

Bürgmann, R., P. A. Rosen, and E. J. Fielding (2000). Synthetic aperture radar interferometry to measure earth's surface topography, *Annu. Rev. Earth Planet. Sci.* **28,** 169–209, doi: 10.1146/annurev.earth.28.1.169.

Charreau, J., Y. Chen, S. A. Gilder, S. Dominguez, J. Lavé, W. M. Wang, and J.-P. Avouac (2009). Neogene uplift of the Tian Shan Mountains observed in the magnetic record of the Jingou River section (northwest China), *Tectonics* **28,** TC2008, doi: 10.1029/2007TC002137.

Chong, J.-H., B. Oryan, L. Shen, M. S. Steckler, and E. O. Lindsey (2024). Interseismic uplift of anticlines above the Rakhine-Bangladesh megathrust from ALOS-2 InSAR, *J. Geophys. Res.* **129,** no. 1, e2023JB030003, doi: 10.1029/2024JB030003.

Contreras, J. (2010). A model for low amplitude detachment folding and syntectonic stratigraphy based on the conservation of mass equation, *J. Struct. Geol.* **32,** no. 4, 566–579, doi: 10.1016/j.jsg.2010.03.006.

Deng, Q. D., P. Z. Zhang, Y. K. Ran, X. P. Yang, W. Min, and Q. Z. Chu (2003). Basic characteristics of active tectonics of China, *Sci. China Earth Sci.* **46,** no. 4, 356–372, doi: 10.1360/03yd9032.

Ding, Y., X. Liu, X. Dai, G. Yin, Y. Yang, and J. Guo (2024). D-InSAR-based analysis of slip distribution and coulomb stress implications from the 2024 M_w 7.01 Wushi earthquake, *Remote Sens.* **16,** no. 22, 4319, doi: 10.3390/rs16224319.

Famiglietti, N. A., D. Cheloni, R. Caputo, and A. Vicari (2025). Geodetic model of the 2024 January 22 M_w 7.0 Wushi (northwestern China) earthquake and M_w 5.7 aftershock from inversion of InSAR data, *Geophys. J. Int.* **241,** no. 2, 941–953, doi: 10.1093/gji/ggaf084.

Fan, Q., C. Xu, L. Yi, Y. Liu, Y. Wen, and Z. Yin (2017). Implication of adaptive smoothness constraint and Helmert variance component estimation in seismic slip inversion, *J. Geod.* **91,** 1163–1177, doi: 10.1007/s00190-017-1015-0.

Fialko, Y., D. Sandwell, M. Simons, and P. Rosen (2005). Three-dimensional deformation caused by the Bam, Iran, earthquake and the origin of shallow slip deficit, *Nature* **435,** no. 7040, 295–299, doi: 10.1038/nature03425.

Fournier, T., M. E. Pritchard, and N. Finnegan (2011). Accounting for atmospheric delays in InSAR data in a search for long-wavelength deformation in South America, *IEEE Trans. Geosci. Remote Sens.* **49,** no. 10, 3856–3867, doi: 10.1109/TGRS.2011.2139217.

Fukuda, J., and K. M. Johnson (2010). Mixed linear-non-linear inversion of crustal deformation data: Bayesian inference of model, weighting and regularization parameters, *Geophys. J. Int.* **181,** 1441–1458, doi: 10.1111/j.1365-246X.2010.04564.x.

Gao, H., M. S. Liao, X. G. Liu, W. B. Xu, and N. Fang (2022). Source geometry and causes of the 2019 Ms 6.0 Changning earthquake in Sichuan, China based on InSAR, *Remote Sens.* **14,** no. 9, 2082, doi: 10.3390/rs14092082.

Goldstein, R. M., and C. L. Werner (1998). Radar interferogram filtering for geophysical applications, *Geophys. Res. Lett.* **25,** no. 21, 4035–4038, doi: 10.1029/98GL02964.

He, Y., T. Li, S. Wen, and C. Wang (2021). The 2020 M_w 6.0 Jiashi earthquake: Coinvolvement of thin-skinned thrusting and basement shortening in shaping the Keping-Tage fold-and-thrust belt in southwestern Tian Shan, *Seismol. Res. Lett.* **92,** no. 6, 3216–3230, doi: 10.1785/0220210063.

Jabbour, M., D. Dhont, Y. Hervouët, and J.-P. Deroin (2012). Geometry and kinematics of fault-propagation folds with variable interlimb angle, *J. Struct. Geol.* **42,** 212–226, doi: 10.1016/j.jsg.2012.05.002.

Jia, L., J. Sun, L. Lü, J. Pang, and Y. Wang (2020). Late Oligocene-miocene intra-continental mountain building of the Harke Mountains, southern Chinese Tian Shan, *J. Asian Earth Sci.* **191,** 104,198, doi: 10.1016/j.jseaes.2019.104198.

Jónsson, S., H. A. Zebker, P. Segall, and F. Amelung (2002). Fault slip distribution of the 1999 M_w 7.1 Hector Mine, California, earthquake, estimated from satellite radar and GPS measurements, *Bull. Seismol. Soc. Am.* **92,** no. 5, 1970–1985, doi: 10.1785/0120000922.

Li, F., X. Cheng, H. Chen, X. Shi, Y. Li, J. Charreau, and R. Weldon (2023). Cenozoic shortening and propagation in the eastern Kuqa fold-and-thrust belt, South Tian Shan, NW China, *Tectonics* **38,** no. 1, e2022TC007447, doi: 10.1029/2022TC007447.

Li, J., Y. Yao, R. Li, S. Yusan, G. Li, J. T. Freymueller, and Q. Wang (2022). Present-day strike-slip faulting and thrusting of the Kepingtage fold-and-thrust belt in southern Tianshan: Constraints from GPS observations, *Geophys. Res. Lett.* **49,** no. 20, e2022GL099105, doi: 10.1029/2022GL099105.

Li, T., J. Chen, J. A. Thompson Jobe, D. W. Burbank, and W. Zheng (2018). Active bending-moment faulting: Geomorphic expression, controlling conditions, accommodation of fold deformation, *Tectonics* **37,** no. 10, 3820–3843, doi: 10.1029/2018TC004982.

Li, T., Z. Chen, J. Chen, J. A. Thompson Jobe, D. W. Burbank, Z. Li, X. He, W. Zheng, P. Zhang, and B. Zhang (2019). Along-strike and downdip segmentation of the Pamir frontal thrust and its association with the 1985 M_w 6.9 Wuqia earthquake, *J. Geophys. Res.* **124,** no. 9, 9890–9919, doi: 10.1029/2019JB017319.

Li, Y., M. Liu, M. Hao, L. Zhu, D. Cui, and Q. Wang (2021). Active crustal deformation in the Tian Shan region, central Asia, *Tectonophysics* **811,** 228,868, doi: 10.1016/j.tecto.2021.228868.

Lü, L., T. Li, Z. Chen, J. Chen, J. Thompson Jobe, and L. Fang (2021). Active structural geometries and their correlation with moderate (M 5.5-7.0) earthquakes in the Jiashi-Keping region, Tian Shan southwestern front, *Seismol. Res. Lett.* **92,** no. 6, 3087–3104, doi: 10.1029/2021TC006760.

Mallick, R., R. Bürgmann, K. Johnson, and J. Hubbard (2021). A unified framework for earthquake sequences and the growth of geological structure in fold-thrust belts, *J. Geophys. Res.* **126,** e2021JB022045, doi: 10.1029/2021JB022045.

Massonnet, D., M. Rossi, C. Carmona, F. Adragna, G. Peltzer, K. Feigl, and T. Rabaute (1993). The displacement field of the landers earthquake mapped by radar interferometry, *Nature* **364,** 138–142, doi: 10.1038/364138a0.

Meng, L. S., C. Yan, S. N. Lv, H. Y. Sun, S. H. Xue, Q. K. Li, L. F. Zhou, D. Edwing, K. Edwing, X. P. Geng, *et al.* (2024). Synthetic aperture radar for geosciences, *Rev. Geophys.* **62,** no. 3, RG2001, doi: 10.1029/2023RG000821.

Metropolis, N., A. W. Rosenbluth, M. N. Rosenbluth, A. H. Teller, and E. Teller (1953). Equation of state calculations by fast computing machines, *J. Chem. Phys.* **21,** 1087–1092, doi: 10.1063/1.1699114.

Molnar, P., and P. Tapponnier (1975). Cenozoic tectonics of Asia: Effects of a continental collision, *Science* **189,** no. 4201, 419–426, doi: 10.1126/science.189.4201.419.

Okada, Y. (1985). Surface deformation due to shear and tensile faults in a half space, *Bull. Seismol. Soc. Am.* **75,** no. 4, 1135–1154, doi: 10.1785/BSSA0750041135.

Qiu, J., J. Sun, and L. Ji (2024). The 2024 M_w 7.1 Wushi earthquake: A thrust and strike-slip event unveiling the seismic mechanisms of the South Tian Shan's thick-skin tectonics, *Remote Sens.* **16,** no. 16, 2937, doi: 10.3390/rs16162937.

Royden, L. H., B. C. Burchfiel, and R. D. van der Hilst (2008). The geological evolution of the Tibetan plateau, *Science* **321,** no. 5892, 1054–1058, doi: 10.1126/science.1155371.

Shen, Z.-K., M. Wang, Y. Li, D. D. Jackson, A. Yin, D. Dong, and P. Fang (2001). Crustal deformation along the Altyn Tagh fault system, western China, from GPS, *J. Geophys. Res.* **106,** no. B12, 607–621, doi: 10.1029/2001JB000349.

Sobel, E. R., and T. A. Dumitru (1997). Thrusting and exhumation around the margins of the western Tarim basin, *J. Geophys. Res.* **102,** no. B3, 5043–5063, doi: 10.1029/96JB03267.

Suppe, J. (1983). Geometry and kinematics of fault-bend folding, *Am. J. Sci.* **283,** no. 7, 684–721, doi: 10.2475/ajs.283.7.684.

Tapponnier, P., and P. Molnar (1979). Active faulting and Cenozoic tectonics of the Tien Shan, *J. Geophys. Res.* **84,** no. B7, 3425–3459, doi: 10.1029/JB084iB07p03425.

Tian, Z., J. Sun, B. F. Windley, Z. Zhang, Z. Gong, X. Lin, and W. Xiao (2016). Cenozoic detachment folding in the southern Tianshan foreland, NW China: Shortening distances and rates, *J. Struct. Geol.* **84,** 142–161, doi: 10.1016/j.jsg.2016.01.007.

Tsukahara, K., and Y. Takada (2018). Aseismic fold growth in southwestern Taiwan detected by InSAR and GNSS, *Earth Planets Space* **70,** 52, doi: 10.1186/s40623-018-0816-6.

Turner, S. A., J. W. Cosgrove, and J. G. Liu (2010). *Controls on Lateral Structural Variability Along the Keping Shan Thrust Belt, SW Tien Shan Foreland, China*, Geological Society of America, London Special Publications, Vol. 348, 71–85, doi: 10.1144/SP348.5.

Turner, S. A., J. G. Liu, and J. W. Cosgrove (2011). Structural evolution of the Piqiang fault zone, NW Tarim basin, China, *J. Asian Earth Sci.* **40,** no. 1, 394–402, doi: 10.1016/j.jseaes.2010.06.005.

Wang, C., L. Chang, X. Wang, B. Zhang, and A. Stein (2024). Interferometric synthetic aperture radar statistical inference in deformation measurement and geophysical inversion: A review, *IEEE Trans. Geosci. Remote Sens.* 12**,** no. 1, 8–35, doi: 10.1109/MGRS.2023.3344159.

Wang, Q., P. Z. Zhang, J. T. Freymueller, R. Bilham, K. M. Larson, X. Lai, and Q. Chen (2001). Present-day crustal deformation in China constrained by global positioning system measurements, *Science* **294,** no. 5542, 574–577, doi: 10.1126/science.1063647.

Wang, S., E. Nissen, L. Pousse-Beltran, T. J. Craig, R. Jiao, and E. A. Bergman (2022). Structural controls on coseismic rupture revealed by the 2020 M_w 6.0 Jiashi earthquake (Kepingtag belt, SW Tian Shan, China), *Geophys. J. Int.* **230,** 1895–1910, doi: 10.1093/gji/ggac159.

Wang, X., C. Xu, Y. Wen, X. Zhao, S. Wang, and G. Xu (2024). Distribution of interseismic coupling along the Maidan fault in Tianshan before the 2024 M_w 7.0 Wushi earthquake, *Geophys. Res. Lett.* **51,** no. 24, e2024GL111472, doi: 10.1029/2024GL111472.

Wells, D. L., and K. J. Coppersmith (1994). New empirical relationships among magnitude, rupture length, rupture width, rupture area, and surface displacement, *Bull. Seism. Soc. Am.* **84,** no. 4, 974–1002, doi: 10.1785/BSSA0840040974.

Wessel, P., J. F. Luis, L. Uieda, R. Scharroo, F. Wobbe, W. H. F. Smith, and D. Tian (2019). The Generic Mapping Tools version 6, *Geochem. Geophys. Geosys.* **20,** 5556–5564, doi:10.1029/2019GC008515.

Wu, C., P. Zhang, Z. Zhang, W. Zheng, B. Xu, W. Wang, Z. Yu, X. Dai, B. Zhang, and K. Zang (2023). Slip partitioning and crustal deformation patterns in the Tianshan orogenic belt derived from GPS

measurements and their tectonic implications, *Earth Sci. Rev.* **238,** 104,362, doi: 10.1016/j.earscirev.2023.104362.

Wu, C., W. Zheng, P. Zhang, Z. Zhang, Q. Jia, J. Yu, H. Zhang, Y. Yao, J. Liu, G. Han, and J. Chen (2019). Oblique thrust of the Maidan fault and late Quaternary tectonic deformation in the southwestern Tian Shan, northwestern China, *Tectonics* **38,** no. 8, 2625–2645, doi: 10.1029/2018TC005248.

Wu, D., Z. Chen, and M. Zimin (2024). InSAR coseismic deformation field and seismogenic structure of the 2020 M_w 6.0 Jiashi earthquake and the implication for the moderate-magnitude seismicity in the southwestern Tian Shan, western China, *Front. Earth Sci.* **11,** 1305519, doi: 10.3389/feart.2023.1305519.

Xiao, W. J., and M. Santosh (2014). The western Central Asian Orogenic Belt: A window to accretionary orogenesis and continental growth, *Gondwana Res.* **25,** no. 4, 1429–1444, doi: 10.1016/j.gr.2013.08.017.

Xiao, W., D. Song, B. F. Windley, J. Li, C. Han, B. Wan, J. Zhang, S. Ao, and Z. Zhang (2020). Accretionary processes and metallogenesis of the central Asian orogenic belt: Advances and perspectives, *Sci. China Earth Sci.* **36,** 329–361, doi: 10.1007/s11430-019-9524-6.

Xu, W., G. Feng, L. Meng, A. Zhang, J. P. Ampuero, R. Bürgmann, and L. Fang (2018). Transpressional rupture cascade of the 2016 Mw 7.8 Kaikoura Earthquake, New Zealand, *J. Geophys. Res.* **123,** no. 3, 2396–2416, doi: 10.1002/2017JB015168.

Yang, S. M., J. Li, and Q. Wang (2008). The deformation pattern and fault rate in the Tianshan Mountains inferred from GPS observations, *Sci. China Earth Sci.* **51,** no. 8, 1064–1080, doi: 10.1007/s11430-008-0090-8.

Yang, X., Q. Deng, P. Zhang, and X. Xu (2008). Crustal shortening of major nappe structures on the front margins of the Tianshan, *Seismol. Geol.* **30,** no. 1, 111–131, (in Chinese with English abstract).

Yang, X., Y. Ran, F. Song, X. Xu, J. Cheng, W. Min, Z. Han, and L. Chen (2006). The analysis for crust shortening of kalpin thrust tectonic zone, south-western Tianshan, Xinjiang, China, *Seismol. Geol.* **28,** no. 2, 194–204 (in Chinese with English abstract).

Yao, Y., S. Wen, T. Li, and C. Wang (2020). The 2020 M_w 6.0 Jiashi earthquake: A fold earthquake event in the southern Tian Shan, northwest China, *Seismol. Res. Lett.* **92,** no. 2A, 859–869, doi: 10.1785/0220200146.

Yin, A., S. Nie, P. Craig, T. M. Harrison, F. J. Ryerson, Q. Xiang, and Y. Geng (1998). Late Cenozoic tectonic evolution of the southern Chinese Tian Shan, *Tectonics* **17,** no. 1, 1–27, doi: 10.1029/97TC03140.

Zelenin, E., D. Bachmanov, S. Garipova, V. Trifonov, and A. Kozhurin (2022). The active faults of Eurasia database (AFEAD): The ontology and design behind the continental-scale dataset, *Earth Syst. Sci. Data* **14,** 4489–4503, doi: 10.5194/essd-14-4489-2022.

Zhang, B., L. Qian, T. Li, J. Chen, J. Xu, Y. Yao, L. Fang, C. Xie, J. Chen, G. Liu, *et al.* (2024). Geological disasters and surface ruptures of the January 23, 2024 Ms7.1 Wushi earthquake, Xinjiang, China, *Seismol. Geol.* **46,** no. 1, 220–234, doi: 10.3969/j.issn.0253-4967.2024.01.013 (in Chinese with English abstract).

Zhang, L., A. Li, X. Yang, W. Huang, S. Li, and H. Yang (2024). Multiple fold earthquakes recorded by the paleoseismic surface ruptures of bending-moment faults in the Qiulitage Anticline, South Tianshan, China, *Seismol. Res. Lett.* **95,** no. 5, 2844–2858, doi: 10.1785/0220230388.

Zhang, P. Z., Z. K. Shen, M. Wang, W. J. Gan, R. Burgmann, P. Molnar, Q. Wang, Z. Niu, J. Sun, J. Wu, H. Sun, and X. You (2004). Continuous deformation of the Tibetan plateau from global positioning system data, *Geology* **32,** no. 9, 809–812, doi: 10.1130/G20554.1.

Zhang, X., J. Li, X. Liu, Z. Li, and N. Adil (2023). Coseismic deformation field and fault slip distribution inversion of the 2020 Jiashi Ms 6.4 earthquake: Considering the atmospheric effect with Sentinel-1 data interferometry, *Sensors* **23,** no. 6, 3046, doi: 10.3390/s23063046.

Zhang, Y., S. Yang, H. Chen, Y. Dilek, X. Cheng, X. Lin, and C. Wang (2019). The effect of overburden thickness on deformation mechanisms in the Keping fold-thrust belt, southwestern Chinese Tian Shan Mountains, *Tectonophysics* **753,** 79–92, doi: 10.1016/j.tecto.2019.01.005.

Zhao, L., Z. Chen, L. Xie, Z. Zhu, and W. Xu (2024). Coseismic deformation and slip model of the 2024 M_W 7.0 Wushi earthquake obtained from InSAR observation, *Rev. Geophys. Planet. Phys.* **55,** no. 4, 453–460, doi: 10.19975/j.dqyxx.2024-010 (in Chinese with English abstract).

Zhao, X., L. Zhou, C. Xu, G. Jiang, W. Feng, Y. Wen, and N. Fang (2024). Modified Bayesian method for simultaneously imaging fault geometry and slip distribution with reduced uncertainty, applied to 2017 M_w 7.3 Sarpol-e Zahab (Iran) earthquake, *J. Geod.* **98,** 106, doi: 10.1007/s00190-024-01906-6.

Zheng, G., H. Wang, T. J. Wright, Y. Lou, R. Zhang, W. Zhang, C. Shi, J. Huang, and N. Wei (2017). Crustal deformation in the India-Eurasia collision zone from 25 years of GPS measurements, *J. Geophys. Res.* **122,** no. 11, 9290–9312, doi: 10.1002/2017JB014465.

Zheng, R., R. Zou, R. Dong, Z. Fang, and Q. Wang (2024). The 2024 M_W 7.0 Wushi earthquake in southern Tianshan convergent zone: Finite-fault model for the coseismic rupture and aftershock, *Seismol. Res. Lett.* **95,** no. 2A, 816–827, doi: 10.1785/0220240126.

Zhou, Y., R. T. Walker, J. Hollingsworth, M. Talebian, X. Song, and B. Parsons (2016). Coseismic and postseismic displacements from the 1978 M_w 7.3 Tabas-e-Golshan earthquake in eastern Iran, *Earth Planet. Sci. Lett.* **452,** 185–196, doi: 10.1016/j.epsl.2016.07.038.

Zubovich, A. V., X.-Q. Wang, Y. G. Scherba, G. G. Schelochkov, R. Reilinger, C. Reigber, O. L. Mosienko, P. Molnar, W. Michajljow, V. I. Makarov, *et al.* (2010). GPS velocity field for the Tien Shan and surrounding regions, *Tectonics* **29,** no. 6, TC6014, doi: 10.1029/2010TC002772.

Manuscript received 30 April 2025
Published online 13 October 2025